REVISION 1

Reduced charge transfer in mixed-spin ferropericlase inferred from its high-pressure refractive index

Lukas Schifferle[1,2], Sergio Speziale[1]; Björn Winkler[3], Victor Milman[4], Sergey S. Lobanov[1,2*]

[1]GFZ German Research Center for Geosciences, Telegrafenberg, 14473 Potsdam, Germany

[2]Institute of Geosciences, University of Potsdam, Karl-Liebknecht-Straße 24-25, 14476 Potsdam, Germany

[3]Institute for Geosciences, Goethe-University Frankfurt, Altenhöferallee 1, 60438 Frankfurt am Main, Germany

[4]Dassault Systèmes BIOVIA, 22 Science Park, Cambridge CB4 0FJ, United Kingdom

*Email: slobanov@gfz-potsdam.de

Supplementary Data

TABLE OF CONTENTS

1. Reflectivity measurements

As illustrated in Figure 1 (main text), we measure reflections from several different interfaces as well as the intensity of light passing through the diamond anvil cell (DAC) to obtain the quantities that are necessary to solve Eq. 1 to 3 (main text). The initial probe intensity in air (I_{air}) was obtained as the amount of light reflected from a reference mirror with 99% reflectivity (I_{mirror}):

$$I_{air} = I_{mirror} / 0.99$$

Measuring the intensity of light reflected from the diamond-air interface we obtain its reflectivity:

$$R_{dia-air} = \frac{I_{dia-air}}{I_{air}}$$

Then, $I_0 = I_{air}(1 - R_{dia-air})$, $I_1 = I_0 R_{dia-smp}$, and $I_2 = I_0 \cdot \left(1 - R_{dia-smp}\right)^2 T^2 R_{dia-smp}$, where $R_{dia\text{-}smp}$ is the reflectivity of the diamond-sample interface and T is the sample transmission. Because samples in DACs are thin (~10 μm), the measured intensity of light reflected from the sample ($I_{dia\text{-}smp}$) always contain contributions from the upstream and downstream diamond-sample interfaces. Coming the above we can write:

$$\frac{I_1 + I_2}{I_0} = R_{dia-smp} + T^2({R_{dia-smp}}^3 - 2{R_{dia-smp}}^2 + R_{dia-smp})$$

Higher order reflections from the diamond-sample interface are not considered in the analysis because their contribution to the measured intensity ratio is negligible (Lobanov et al., 2022). Finally, sample transmission is expressed as:

$$\frac{I_T}{I_{noDAC}} = T({R_{dia-smp}}^2 - 2R_{dia-smp} + 1)(1 - R_{dia-air})^2,$$

where I_T and I_{noDAC} are measured in transmission as graphically defined in Figure 1.

2. Diamond-ferropericlase interface reflectivity values

As discussed the main text and in Schifferle et al. (2022), we assumed a pressure independent refractive index of diamond. If in the future more precise estimations of the high-pressure index of diamond become available, data provided in **Supplementary Table 1** allows to recalculating the refractive index of ferropericlase as well as its absorption coefficient.

Supplementary Table 1: Diamond-sample interface reflectivity ($R_{dia\text{-}smp}$), sample refractive index at λ = 600 nm (n_{smp}), sample transmission (T, not normalized for sample thickness) and apparent thickness (OP, *i.e.,* optical path; real thickness = OP/n_{smp}) as measured in this work, relying on the Fresnel equation for perpendicularly incident light for the assumption n_{dia} = 2.418 and pressure independence of n_{dia}. The values in parentheses are the estimated relative uncertainties on the parameters. Abbreviations: CP = compression, DC = decompression.

Sample	Run#, culet size, pressure path	Pressure [GPa] (±5%)	$R_{dia\text{-}smp}$ (±5%)	n_{smp} (for n_{dia} = *constant* = 2.418) (±1%)	T (±3%)	OP [μm] (err. <1%)
Fp13	100_1, CP	19.8	-	-	0.526	17.967
		20.9	-	-	0.526	17.911
		24.6	-	-	0.469	17.796
		29.2	-	-	0.402	17.412
		33.9	0.02071	1.810	0.356	17.134
		42.9	0.01975	1.822	0.279	16.491
		48.6	0.01941	1.827	0.229	16.122
		52.8	0.01902	1.832	0.197	15.685
		56.6	0.01944	1.826	0.194	15.092

Sample	Run#, culet size, pressure path	Pressure [GPa] (±5%)	$R_{dia\text{-}smp}$ (±5%)	n_{smp} (for n_{dia} = *constant* = 2.418) (±1%)	T (±3%)	OP [µm] (err. <1%)
		63.8	0.01812	1.844	0.217	14.463
		67.2	0.01917	1.830	0.237	13.990
		68.3	0.01918	1.830	0.250	13.849
		70.5	0.01701	1.860	0.268	13.641
		81.5	0.01922	1.829	0.334	13.220
		92.2	0.01871	1.836	0.383	12.861
		96.9	0.0178	1.849	0.376	12.664
		103.5	0.01748	1.853	0.399	12.516
		106.2	0.01862	1.837	0.391	12.539
		111.8	0.01851	1.839	0.406	12.443
		119	0.0184	1.840	0.405	12.342
		129.5	0.01854	1.838	0.415	12.285
		138.4	0.01857	1.838	0.401	12.231
Fp13	100_1, DC	100.4	0.01898	1.832	0.407	12.422
		84.7	0.01946	1.826	0.426	11.906
		75.1	0.01953	1.825	0.403	11.556
		68.6	0.02095	1.807	0.368	11.171
		57	0.02063	1.811	0.344	10.802
		38.6	0.02089	1.807	0.438	9.775
		25.3	-	-	0.569	9.225
		16	-	-	0.647	8.950
		9.9	-	-	0.698	8.921
		7.8	-	-	0.729	8.984
Fp13	100_2, CP	18.7	-	-	0.518	18.676
		26.3	-	-	0.383	18.161
Fp13	100_3, CP	16.9	-	-	0.480	21.537
		19.8		-	0.445	21.216
		23	-	-	0.399	20.898
		28.1	-	-	0.346	19.985
		35	0.02034	1.814	0.264	18.679
		38.2	0.02025	1.816	0.237	18.136
		43.6	0.0201	1.817	0.221	16.789
		50.3	0.01992	1.820	0.195	15.769
		54.9	0.0198	1.821	0.183	14.999
		62.1	0.01961	1.824	0.205	14.267
		69.3	0.01942	1.827	0.258	13.640
		76.2	0.01923	1.829	0.307	13.276
		82.8	0.01906	1.831	0.341	12.887
		86.9	0.01895	1.833	0.366	12.868
		89.7	0.01888	1.834	0.385	12.751
		100.3	0.01861	1.838	0.391	12.417
		109.1	0.01838	1.841	0.403	12.601

Sample	Run#, culet size, pressure path	Pressure [GPa] (±5%)	$R_{dia\text{-}smp}$ (±5%)	n_{smp} (for n_{dia} = *constant* = 2.418) (±1%)	*T* (±3%)	*OP* [µm] (err. <1%)
Fp13	300_1, CP	34.8	0.01984	1.821	0.064	37.384
Fp24	100_1, CP	24.8	0.01864	1.837	0	-
		31.1	0.01816	1.844	0	-
		40.8	0.01777	1.849	0	-
		48.9	0.01766	1.851	0	-
		58.4	0.01721	1.857	0	-
		61.5	0.01716	1.858	0	-
		66.6	0.01756	1.852	0	-
		73.9	0.01752	1.853	0	-
		88.6	0.01716	1.858	0	-
		99.5	0.01697	1.861	0	-
		105	0.01651	1.867	0	-
Fp24	100_1, DC	94.1	0.01682	1.863	0	-
		77.7	0.0172	1.857	0	-
		65.7	0.01704	1.860	0	-
		55.2	0.01644	1.868	0	-
		50.7	0.01665	1.865	0	-
		45.4	0.01689	1.862	0	-
		38.8	0.01725	1.857	0	-
		31.6	0.01757	1.852	0	-
		28.2	0.01758	1.852	0	-
		21.9	0.01744	1.854	0.005	10.218
		19.1	0.0178	1.849	0.014	10.544
		14.3	0.01783	1.848	0.027	10.561
		11.04	0.01766	1.851	0.039	10.478
		8.7	0.01777	1.849	0.053	10.442
		5.5	0.01877	1.835	0.075	10.416

3. Compositional dependence of ferropericlase refractive index

Ambient pressure measurements of Henning et al. (1995) allow an estimation of the refractive index n(600 nm) of our Fp13 and Fp24 samples. A 2nd order polynomial fit to their data (lowest reported Fe content therein, $(Mg_{0.60}Fe_{0.40})O$) yields $n(x_{Fe}) = 4.675 \cdot 10^{-5}(\pm 9.444 \cdot 10^{-5}) \cdot {x_{Fe}}^2 + 0.0024\ (\pm 0.0133) \cdot x_{Fe} + 1.751\ (\pm 0.428)$ at 600 nm. As shown in **Figure S1** (dotted line), our experimental data fit a 2nd order polynomial trend well. A revised fit of the compositional dependence of the refractive index to the iron content is shown by the solid trendline in **Figure S1**: $n(X_{Fe}) = 4.286{\cdot}10^{-5}(\pm 2.144{\cdot}10^{-5}){\cdot}{X_{Fe}}^2 + 0.003(\pm 0.002){\cdot}X_{Fe} + 1.739(\pm 0.047)$.

While there are still unanswered questions on the low-pressure behavior of $n(600\ nm)$, our high-pressure data is suitable for first in-situ thickness measurements and the calculation of

absorption coefficients. To reduce the influence of experimental uncertainties, for the calculation of the absorption coefficient, we derive a near-linear relationship of the refractive index n(600 nm) of ferropericlase with pressure. For Fp13 we find $n_{Fp13} = 3.535 \cdot 10^{-4}(\pm 7.022 \cdot 10^{-5}) \cdot P + 1.802(\pm 0.006)$ and $n_{Fp24} = 2.042 \cdot 10^{-4}(\pm 3.920 \cdot 10^{-5}) \cdot P + 1.844(\pm 0.002)$ (P is expressed in GPa; both fits including only data where $P > 30$ GPa).

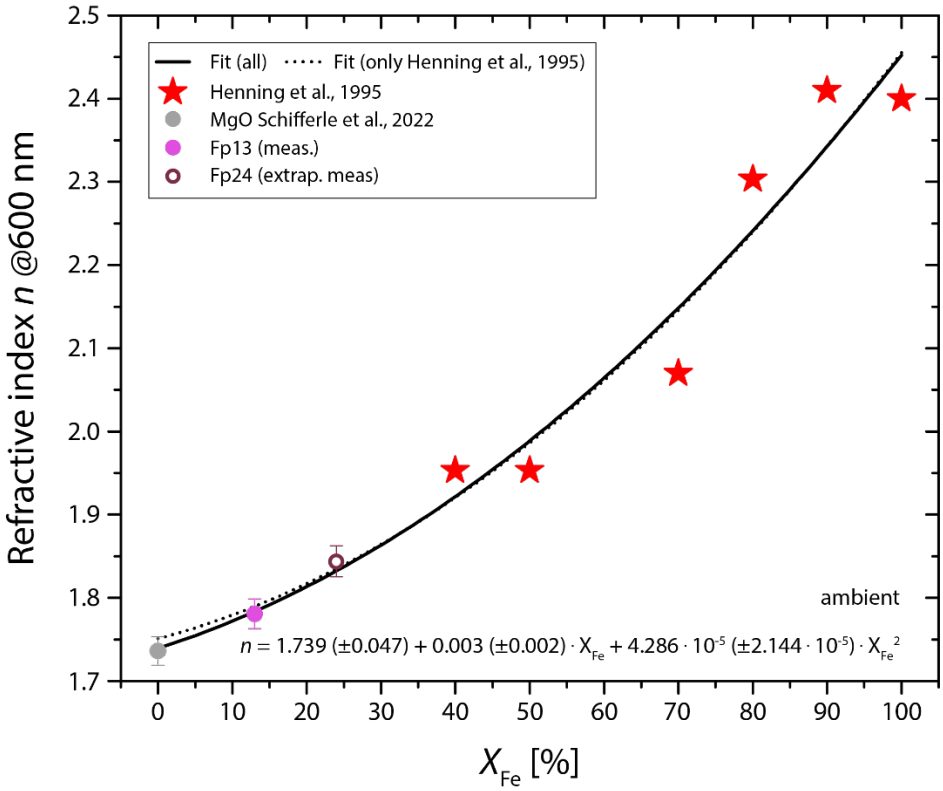

Figure S1: Dependence of the ambient pressure refractive index on the iron content, based on this work (Fp13, Fp24), data of Henning et al. (1995) ((Mg,Fe)O) and Schifferle et al. (2022) (MgO). Solid trendline and equation represent all datasets shown, dotted line uses only data reported by Henning et al. (1995).

4. Polarizability of ferropericlase at high pressure

The Lorenz-Lorentz polarizability, α_{LL} was calculated as in our previous MgO paper (Schifferle et al., 2022):

$$\alpha_{LL} = \frac{3M(n^2 - 1)}{\rho 4\pi(n^2 + 2)}$$

where M is the molecular weight of MgO and Fp17 (40.3044 and 45.6662 g/mol), ρ the pressure-dependent density calculated from the equation of state of MgO (Tange et al., 2009) or using the data reported by Lin et al. (2005) and Solomatova et al. (2016). Please note here that we have to use these reports on ferropericlase density at high pressure because no equation of state data is available for Fp13. The refractive index (n) of Fp17 is assumed to be 0.96 %

higher than Fp13 (based on our estimation of the compositional dependence of the index (Fig. S1)).

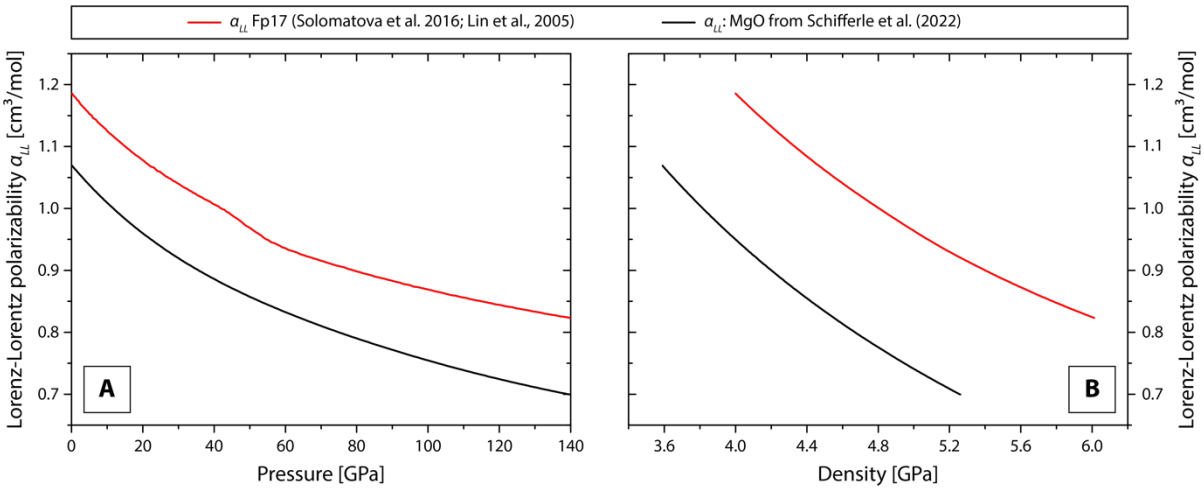

Figure S2. Lorenz-Lorentz polarizability of $(Mg_{0.83}Fe_{0.17})O$ (Fp17) as a function of pressure (**A**) and density (**B**).

5. High-pressure sample geometry and absorption coefficient

Our setup for refractive index measurements is not designed for broad-band spectral measurements (max. ~400-900 nm). Those, however, are necessary for the use in radiative conductivity calculations (e.g. Goncharov et al. (2006)). Therefore, we used our α(600 nm) for Fp13 (main text, **Figure 3**), to derive a wide-range absorption coefficient from previously published absorbance data of Schifferle and Lobanov (2022) (**Figure S A**), which was performed on a piece of the exact same Fp13 crystal. This was done by multiplying the absorbance data of Schifferle and Lobanov (2022) by a scalar, derived as $\frac{\alpha(600\ nm)}{A(600\ nm)}$. In the mixed-spin region, a reduction of the absorption coefficient in the range λ < 600 nm is observed. Towards the full low-spin state, the sample's UV-transparency is highly increased. The wavelength-dependent absorption coefficient (α(λ)) is directly related to the imaginary part of the refractive index (κ): $\kappa = (\lambda \cdot \alpha(\lambda))/(4 \cdot \pi)$. Hence, the observed trends in κ are similar as for α (**Figure S B**). Especially for λ < 600 nm, κ in the full-low spin state is vastly different from high-spin or mixed-spin. High κ for λ > 1000 nm observed for 81 and 105 GPa is probably related to instrumental errors for these two pressure points.

By analyzing the fringe pattern from the center and periphery of the sample, we constrain the thinning of the sample area on compression and decompression for Fp13 100 run 3 to a maximum pressure of ~109 GPa (**Figure S**). The observed thinning is far more pronounced than the isotropic compression/expansion, where $\frac{d}{d_0} = \left(\frac{V}{V_0}\right)^{1/3}$, with V and V_0 as the high-pressure and 1 atm unit cell volume and d and d_0 the according thicknesses, from the EoS would suggest (Mao et al., 2011; Wentzcovitch et al., 2009; Yang et al., 2015) (i.e., samples

are up to 50% thinner on compression than expected from the EOS). See also Lobanov and Geballe (2022) for a thorough discussion. For the calculation of our thickness, we used the linear pressure dependence of the refractive index in Fp13. We find a decreasing thickness of the sample down to ~90 GPa. It is noted that the relative difference of thickness in center and periphery increases from 0.7% at ~17 GPa to 3.6% at ~109 GPa, which we assign to the diamond cupping at high-pressure (Li et al., 2018; Mao and Mao, 2007). Based on a 2nd order polynomial fit (dashed line in **Figure S**) we estimate sample thickness at 1 atm of ~14.54 μm. The 1 atm (theoretical) thickness is then used to calculate relative thinning of the sample. From 1 atm to ~109 GPa we find a thinning by ~50%.

On decompression, we observe further thinning of the sample, down to ~65% (from 1 atm). This is accompanied by substantial radial growth of the sample area. At P < 10 GPa we observe an increase of sample thickness, which was also confirmed by a FIB cross-section through the center of the decompressed sample (main Text, **Figure 1 D**). Similar compression/decompression thinning has been observed previously (Dewaele et al., 2003; Kalkan et al., 2012; Lobanov and Geballe, 2022).

The decrease of diamond culets' cupping in decompression leads to large radial strain in the sample and a push-down effect at the culet center which causes the reduction of sample thickness (**Figure S**, **A**). Such a process is consistent with the decreasing in edge-center thickness difference (**Figure S**). The irregular outline of the sample (**Error! Reference source not found.**main text, **Figure 1 D**) is likely a product of heterogeneous radial strain gradients (**Figure S**, **B**). As visible in the cross-section, displacement is less dominant at the interface to the diamond culet, creating an overlap of gasket material over the sample. Please note, this is only a decompression feature. Walls of the DAC sample chamber stay visibly vertical on compression, as is also indicated by sharp edges of x-ray transmission data of previous studies(Dewaele et al., 2018; Dong et al., 2021; Lamichhane et al., 2021). We propose, on decompression high friction at the diamond-sample and at the diamond-gasket interfaces results in a non-uniform relative displacement field as illustrated in **Figure S B**. Thickness increase observed at low pressure could reflect the final elastic rebound of the sample.

Although our transmission measurements on Fp24 are limited, **Figure 3** (main text) shows that the absorption coefficient of ferropericlase is strongly non-linear and dominated by the iron content (factor of ~13 difference at 10 GPa between Fp13 and Fp24). Similar conclusions were also drawn by Deng et al. (2017). Unfortunately, the absorption mechanisms caused by the iron-iron interactions are difficult for DFT to consider. Hence, experiments are inevitable to assess the composition, pressure, and wavelength-dependence of the absorption coefficient.

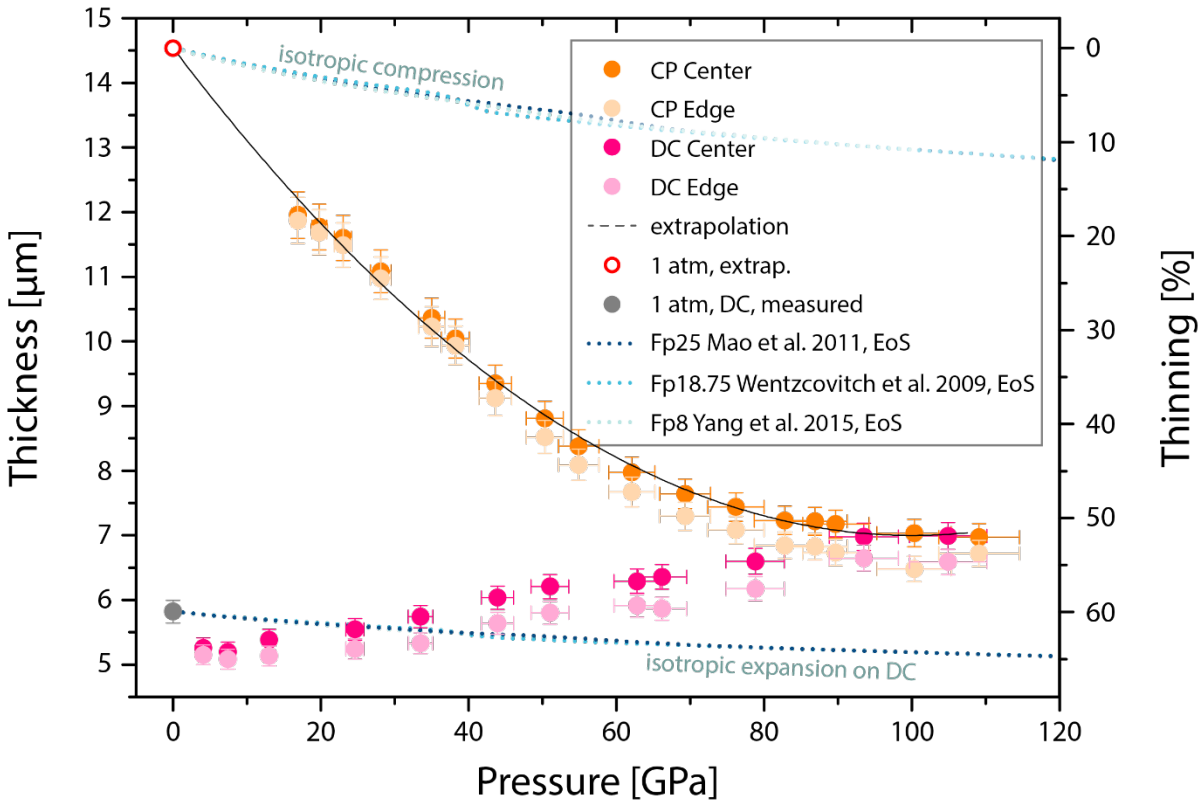

Figure S3 Sample thickness on compression and decompression of Fp13 100 run 3. Dashed line is a 2nd order polynomial fit to the compression data and is used to extrapolate thickness at 1 atm (empty red circle). Grey circle marks the measured thickness of the decompressed sample center from a FIB cross section. CP = compression, DC = decompression. Dotted lines show a theoretical isotropic compression/expansion based on the isothermal equation of state (EoS) for Fp25 (Mao et al., 2011), Fp18.75 (Wentzcovitch et al., 2009) and Fp8 (Yang et al., 2015).

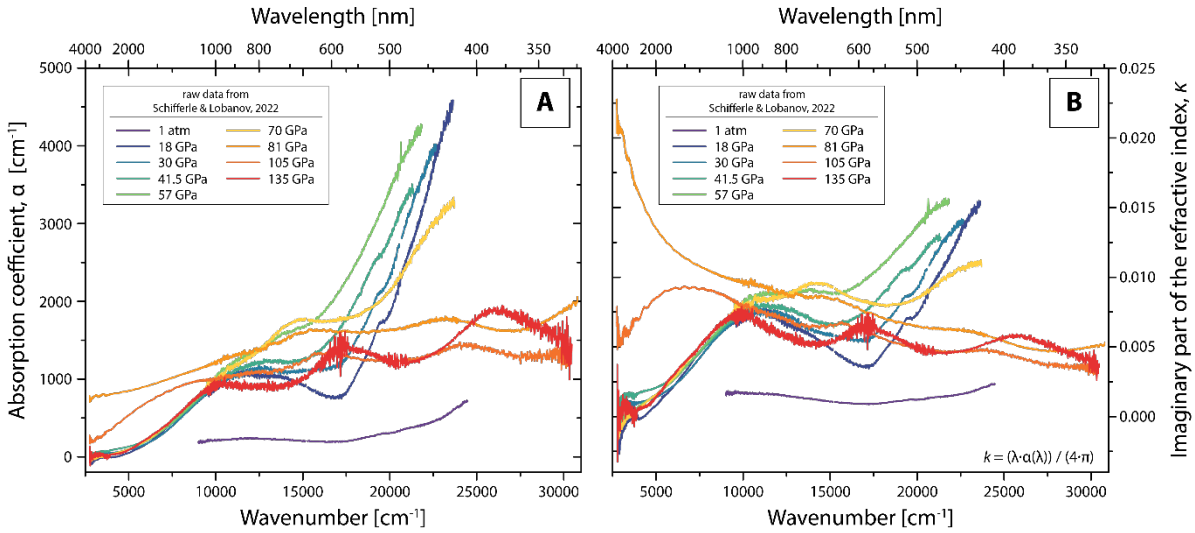

Figure S4: Absorption coefficient (α) (**A**) and imaginary part of the refractive index (κ) for Fp13 (**B**), based on absorption data of Schifferle and Lobanov (2022).

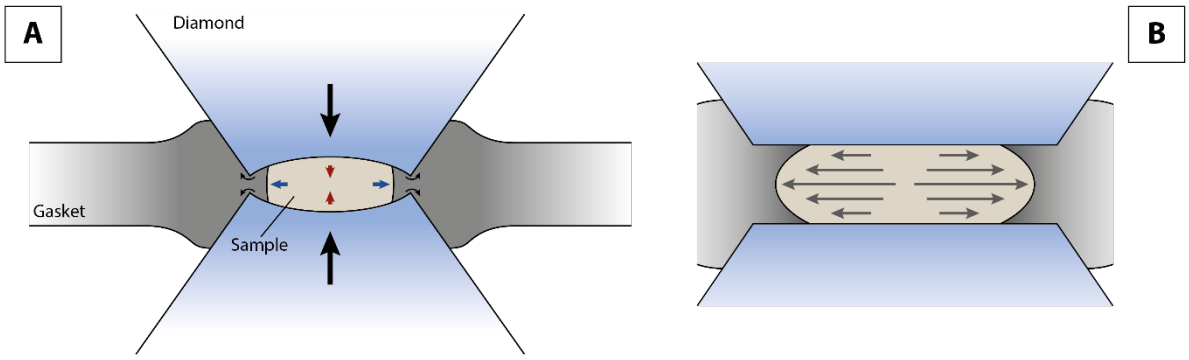

Figure S5 A: Geometry change of cupped diamonds and sample on decompression. Black arrows represent diamond movement, blue arrows indicate enlargement for the sample, red arrows shrinking of the sample. **B**: Schematic displacement field of the sample.

6. References

Deng, J., Du, Z., Benedetti, L.R., and Lee, K.K.M. (2017) The influence of wavelength-dependent absorption and temperature gradients on temperature determination in laser-heated diamond-anvil cells. Journal of Applied Physics, 121(2), 025901.

Dewaele, A., Eggert, J.H., Loubeyre, P., and Le Toullec, R. (2003) Measurement of refractive index and equation of state in dense He, H2, H2O, and Ne under high pressure in a diamond anvil cell. Physical Review. B, Condensed matter, 67(9).

Dewaele, A., Loubeyre, P., Occelli, F., Marie, O., and Mezouar, M. (2018) Toroidal diamond anvil cell for detailed measurements under extreme static pressures. Nature Communications, 9(1), 2913.

Dong, W., Glazyrin, K., Khandarkhaeva, S., Fedotenko, T., Bednarčík, J., Dubrovinsky, L., Dubrovinskaiac, N., and Liermann, H.-P. (2021) Fe0.79Si0.07B0.14 metallic glass gaskets for high-pressure research beyond 1 Mbar.

Goncharov, A.F., Struzhkin, V.V., and Jacobsen, S.D. (2006) Reduced radiative conductivity of low-spin (Mg,Fe)O in the lower mantle. Science, 312(5777), 1205–1208.

Henning, T., Begemann, B., Mutschke, H., and Dorschner, J. (1995) Optical properties of oxide dust grains. Astronomy & Astrophysics Supplement Series, 112, 143–149.

Kalkan, B., Sonneville, C., Martinet, C., Champagnon, B., Aitken, B.G., Clark, S.M., and Sen, S. (2012) Hysteretically reversible phase transition in a molecular glass. The Journal of Chemical Physics, 137(22), 224503.

Lamichhane, A., Kumar, R., Ahart, M., Salke, N.P., Dasenbrock-Gammon, N., Snider, E., Meng, Y., Lavina, B., Chariton, S., Prakapenka, V.B., and others. (2021) X-ray diffraction and equation of state of the C-S-H room-temperature superconductor. The Journal of Chemical Physics, 155(11), 114703.

Li, B., Ji, C., Yang, W., Wang, J., Yang, K., Xu, R., Liu, W., Cai, Z., Chen, J., and Mao, H.-K. (2018) Diamond anvil cell behavior up to 4 Mbar. Proceedings of the National Academy of Sciences of the United States of America, 115(8), 1713–1717.

Lin, J.F., Struzhkin, V.V., Jacobsen, S.D., Hu, M.Y., Chow, P., Kung, J., Liu, H.Z., Mao, H.K., and Hemley, R.J. (2005) Spin transition of iron in magnesiowustite in the Earth's lower mantle. Nature, 436(7049), 377-380.

Lobanov, S.S., and Geballe, Z.M. (2022) Non-isotropic contraction and expansion of samples in diamond anvil cells: Implications for thermal conductivity at the core-mantle boundary. Geophysical Research Letters, 49(19), e2022GL100379.

Lobanov, S.S., Speziale, S., Winkler, B., Milman, V., Refson, K., and Schifferle, L. (2022) Electronic, Structural, and Mechanical Properties of SiO_2 Glass at High Pressure Inferred from its Refractive Index. Physical Review Letters, 128(7), 077403.

Mao, H.-K., and Mao, W.L. (2007) Theory and practice – ciamond-anvil cells and probes for high P–T mineral physics studies. In G.D. Price, and G. Schubert, Eds. Treatise on Geophysics, 2, p. 231–267. Elsevier.

Mao, Z., Lin, J.F., Liu, J., and Prakapenka, V.B. (2011) Thermal equation of state of lower-mantle ferropericlase across the spin crossover. Geophysical Research Letters, 38(23), L23308.

Schifferle, L., and Lobanov, S.S. (2022) Evolution of chemical bonding and spin-pairing energy in ferropericlase across its spin transition. ACS Earth and Space Chemistry, 6(3), 788–799.

Schifferle, L., Speziale, S., and Lobanov, S.S. (2022) High-pressure evolution of the refractive index of MgO up to 140 GPa. Journal of Applied Physics, 132(12), 125903.

Solomatova, N.V., Jackson, J.M., Sturhahn, W., Wicks, J.K., Zhao, J.Y., Toellner, T.S., Kalkan, B., and Steinhardt, W.M. (2016) Equation of state and spin crossover of (Mg,Fe)O at high pressure, with implications for explaining topographic relief at the core-mantle boundary. American Mineralogist, 101(5-6), 1084-1093.

Tange, Y., Nishihara, Y., and Tsuchiya, T. (2009) Unified analyses for P-V-T equation of state of MgO: A solution for pressure-scale problems in high P-T experiments. Journal of Geophysical Research-Solid Earth, 114, B03208.

Wentzcovitch, R.M., Justo, J.F., Wu, Z., Da Silva, C.R.S., Yuen, D.A., and Kohlstedt, D. (2009) Anomalous compressibility of ferropericlase throughout the iron spin cross-over. Proceedings of the National Academy of Sciences of the United States of America, 106(21), 8447–8452.

Yang, J., Tong, X., Lin, J.F., Okuchi, T., and Tomioka, N. (2015) Elasticity of ferropericlase across the spin crossover in the Earth's lower mantle. Scientific Reports, 5, 17188.